







Mechanism of stable lithium plating and stripping in a metal-interlayer-inserted anode-less solid-state lithium metal battery

Received: 1 May 2024

Accepted: 20 December 2024

Published online: 27 January 2025



Dong-Su Ko ^{1,5}✉, Sewon Kim ^{2,5}, Sangjun Lee¹, Gabin Yoon ², Daeho Kim³, ChaeHo Shin⁴, Dongmin Kim¹, Jaewoo Lee¹, Soohwan Sul ¹, Dong-Jin Yun ¹✉ & Changhoon Jung ¹✉

To reliably operate anode-less solid-state Li metal batteries, wherein precipitated Li acts as the anode, stabilizing the interface between the solid electrolyte and electrode is crucial. The interface can be controlled by a metal interlayer on the electrolyte to form a Li alloy buffer that facilitates stable Li plating/stripping, thereby mitigating the loss of physical contact and preventing short circuits. However, the mechanism governing stable Li plating/stripping in the metal interlayer without degrading battery materials remains unclear owing to an incomplete understanding of the dynamic and complex electrochemical reactions in the solid state. Through multiple *operando* and *post-mortem* analyses of the Li deposition behavior in the morphology, chemistry and microstructure, a close correlation is found between the Li-metal alloying process with the microstructural evolution and electrochemical performance when Ag, Au, Zn, and Cu interlayers were adopted on the garnet-type solid electrolyte $\text{Li}_{6.5}\text{La}_3\text{Zr}_{1.5}\text{Ta}_{0.5}\text{O}_{12}$. The Ag interlayer improved the interfacial stability enabled by Ag-dissolved Li, which inhibited dendritic growth, passing through the phase-separated Li-Ag alloy microstructure, while the other metals did not because of the Li plating at the Li-metal alloy/solid electrolyte interface. This work provides fundamental guidance for material selection and interface design, advancing the development of anode-less solid-state batteries.

Li metal batteries (LMBs) have attracted considerable attention as next-generation batteries due to their higher energy densities than those of current Li-ion batteries (LIBs)^{1–3}. However, the safety issue hinders their practical application in commercial products^{4,5}. The adoption of solid electrolytes instead of liquid electrolytes, thereby creating solid-state LMBs (SS-LMBs), has emerged as a promising solution to mitigate the challenges associated with conventional LMBs.

Numerous studies have indicated the high performances of SS-LMBs^{6,7}. Nevertheless, considering practical battery manufacturing, the application of Li metal as an anode is challenging owing to the intricate process and associated costs involved in handling Li metal. As a revolutionary solution to address this challenge, anode-less SS-LMBs (AL-SS-LMBs) have been proposed, and their efficacies have been demonstrated^{8–11}. As AL-SS-LMBs utilize precipitated Li metal as the

¹Analytical Engineering Group, Samsung Advanced Institute of Technology, 130 Samsung-ro, Yeongtong-gu, Suwon-si, Gyeonggi-do, Republic of Korea.

²Battery Materials Technical Unit, Samsung Advanced Institute of Technology, 130 Samsung-ro, Yeongtong-gu, Suwon-si, Gyeonggi-do, Republic of Korea.

³Division of Chemical and Material Metrology, Bruker Korea, 338 Pangyo-ro, Bundang-gu, Seongnam-si, Gyeonggi-do, Republic of Korea. ⁴Division of Industrial Metrology, Korea Research Institute of Standards and Science, 267 Gajeong-ro, Yuseong-gu, Daejeon, Republic of Korea. ⁵These authors contributed equally: Dong-Su Ko, Sewon Kim. ✉e-mail: ds02.ko@samsung.com; dongjin.yun@samsung.com; ch1.jung@samsung.com

anode and the Li source is solely relied on the cathode, handling of Li metal is not required throughout battery manufacturing. Furthermore, AL-SS-LMBs not only reduce both material and process costs, but also demonstrate substantially high energy densities due to a decrease in anode volume caused by the removal of the pre-existing Li metal source^{2,12}. Hence, the development of AL-SS-LMBs represents a promising advancement in energy storage technology, offering the potential for higher energy densities and improved safety compared to conventional batteries. However, a critical challenge that hampers their practical implementation is ensuring the interfacial stability between the solid electrolyte and the electrode, particularly given that the precipitated Li itself serves as the anode. A stable interface is essential to prevent issues such as the loss of physical contact area and the formation of short circuits, both of which can significantly degrade battery performance and reliability. One promising approach to achieving this stability is the introduction of metal interlayers on the solid electrolyte^{13–17}. These interlayers function as buffer layers by forming Li alloys, thereby facilitating stable Li plating and stripping. This approach has shown promise in mitigating the detrimental effects associated with the interface, paving the way for more reliable operation of anode-less solid-state Li metal batteries^{18–21}. However, despite these advancements, the fundamental mechanisms governing stable Li plating and stripping within the metal interlayer remain poorly understood. The lack of a comprehensive understanding of the dynamic and complex electrochemical reactions in the solid state, without the degradation of battery materials, presents a significant barrier to optimizing these systems.

Recently, Lee et al. efficiently cycled an AL-SS-LMB over 1,000 times with an outstanding energy density of 900 Wh·L⁻¹ by effectively controlling the interface on the solid electrolyte²². They exhibited repetitive, dense Li plating and stripping with respect to battery charging and discharging, and Li plating and stripping were facilitated by introducing a Ag-C composite layer at the interface between the sulfide electrolyte and current collector. This achievement represents a pivotal development, prompting numerous subsequent studies aimed at unraveling the fundamental operational principles behind the Ag-C composite layer^{23,24}. Via computational and experimental analyses, the C component in the Ag-C interlayer has been revealed to induce Li plating on the current collector surface, thus preventing undesirable Li plating on the solid electrolyte surface, and to improve the uniformity of the current distribution at the interface^{23–25}. Meanwhile, Ag has been studied to elucidate its function in the composite layer and various metals have been explored as alternatives to Ag to improve the performance of this composite layer²⁶. Ag acts as a seed for the preferential precipitation of Li metal as compared to the cases of several other metal nanoparticles, facilitating a more uniform distribution of the precipitated Li metal. Similarly, Kim et al. indicated the viabilities of AL-SS-LMBs employing the garnet-type oxide electrolyte Li₇La₃Zr₂O₁₂ by incorporating a thin Ag interlayer into the electrolyte surface²⁷. They reported that homogeneous Li plating and stripping enabled by the Ag interlayer played a critical role in the enhancement of battery performances, whereas other metal layers, such as Si and Au layers, led to inferior battery performances due to inhomogeneous Li metal precipitation. The advantages of the Ag interlayer in AL-SS-LMBs have been further verified in succeeding studies²⁸.

Nevertheless, the mechanism governing the electrochemical lithiation of Ag in solid-state battery systems and the correlation between this lithiation process and the enhanced battery performance remain unknown. Hence, elucidating the fundamental mechanism of interlayer lithiation is crucial to achieving stable Li plating and stripping in AL-SS-LMBs.

Although several studies have suggested the role of a metal interlayer in stabilizing Li plating and stripping, most have been limited to liquid-electrolyte LIB systems, wherein the nucleation and growth of Li metal in the solid solution of Li-metal alloy occurs toward the liquid

electrolyte. These findings are therefore difficult to apply to solid-state battery systems^{29,30}. Inaoka et al. reported that metals that do not have solid solubility in Li can sustain a stable interlayer between the Li-metal anode and the solid electrolyte³¹. However, the roles of metal interlayers remained unresolved.

Furthermore, as most experiments have been conducted using *post-mortem* analysis, the reacted Li metal, which is very sensitive to air exposure, could not be reserved in the actual reaction state. Recently, to circumvent these issues, various state-of-the-art *operando* analytical techniques without air exposure have been developed and applied to elucidate the mechanisms of Li plating and stripping at solid/solid interfaces. However, stand-alone analysis is not sufficient to provide a comprehensive understanding of the electrochemical, morphological, microstructural, and chemical changes occurring during battery operation.

In this study, we investigate the effectiveness of various metal interlayers, specifically Ag, Au, Zn, and Cu, in enhancing the interfacial stability of these batteries, with a focus on their role in maintaining physical contact and preventing short circuits. By conducting multiple *operando* and *post-mortem* analyses of Li deposit behaviors, we successfully examined the evolution of the morphology, chemistry, and microstructure of the Li deposits and uncovered a close correlation between the Li-metal alloying process, microstructural evolutions, and electrochemical performance. Our findings reveal a significant correlation between the Li-metal alloying process, microstructural changes, and the electrochemical performance when these metal interlayers are employed. Notably, the Ag interlayer stands out for its ability to enhance interface stability. This is achieved through a unique phase transition during Li-Ag alloying, and Ag-dissolved Li plating, which mitigates dendritic growth. In contrast, other metal interlayers such as Au, Zn, and Cu do not exhibit the same level of effectiveness due to non-uniform/dendritic Li plating occurring at the Li-metal alloy/solid electrolyte interface, leading to less stable performance.

Results and Discussion

Morphological and chemical evolution during Li plating and stripping

Li metal and its compounds are very sensitive to oxygen and moisture in the atmosphere, facilitating their morphological and chemical degeneration. Thus, the environment in which experiments are performed must be tightly controlled to avoid artifacts in *operando* and *post-mortem* observations. This study adopts a remote-gate-controlled airtight transfer vessel modified to enable battery cycling for *operando* SEM and XPS to prevent air exposure during the transfer of batteries between analytical instruments (Supplementary Figs. 1 and 2). Coupled with this airtight transfer, *operando* SEM was conducted on four different metal||LLZO||Li cells during galvanostatic cycling at 0.1 mA cm⁻². In each cell, a 200-nm-thick metal interlayer (Ag, Zn, Au, or Cu) was deposited on the LLZO electrolyte surface as the anode interlayer, and the morphological evolution of each interlayer was traced during Li plating and stripping during (Fig. 1a and Supplementary Fig. 3). For simplicity, cells are hereafter denoted by their metal interlayer. The coulombic efficiencies of the cells were obtained using *operando* measurements and increased in the following order: Cu interlayer cell < Au interlayer cell < Zn interlayer cell < Ag interlayer cell. In addition, several voltage plateaus arising from Li-metal alloy production/transformation were observed during Li plating/stripping for all metal interlayer cells except for the Cu interlayer cell. Morphological changes, including the intermediate process during Li plating and stripping, are systematically depicted in Supplementary Movies 1–5. As shown in the *operando* SEM images, the surface morphology exhibits different features depending on the type of metal interlayer, and thus, it will be explained by dividing it into two types based on whether an alloy is formed with Li or not. Reduction of Li⁺ should mainly occur at the metal/LLZO interface. In the case of the Cu interlayer cell, Li deposits

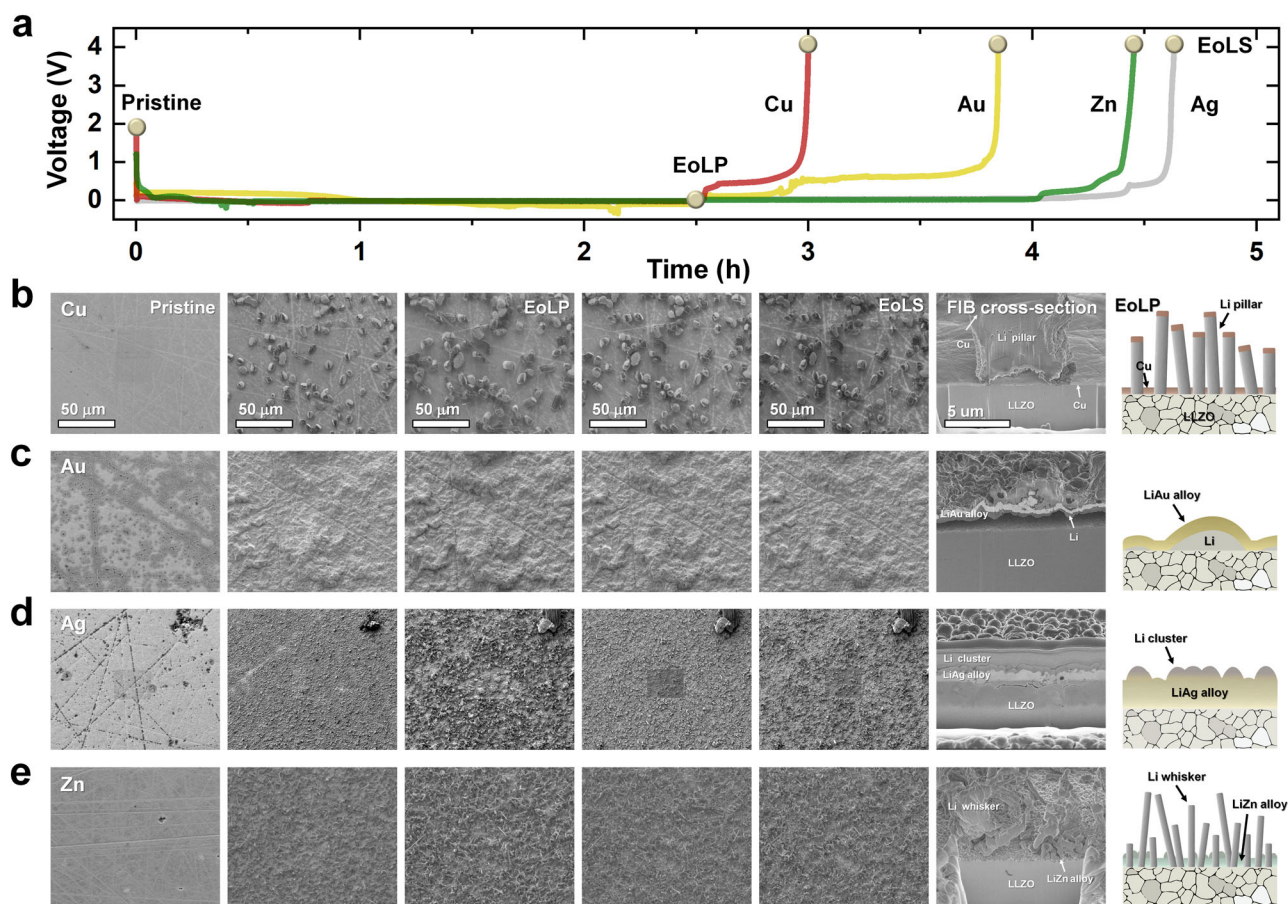


Fig. 1 | Operando SEM of metal | LLZO | Li cells. a Charge/discharge profiles and corresponding SEM images of **(b)** Cu, **(c)** Au, **(d)** Ag, and **(e)** Zn interlayer cells with schematics of the cross-sectional morphologies at EoLP. Note that the same scale

bars are used in all SEM images of **(b–e)**, whereas different scale bars are employed for the FIB cross-section images.

can be predicted to be plated underneath the Cu interlayer because Cu does not alloy with Li. For the same reason, Cu has been used as a current collector metal for Li-based batteries. Herein, the Cu interlayer was employed as a control parameter with or without other metal interlayers to demonstrate general Li plating/stripping on the LLZO surface. In Fig. 1b and Supplementary movie 2, during Li plating, the features of surface morphology change as follows: metallic Li deposits initially grow laterally to diameters of ~15 μm and then vertically grow into pillars, and simultaneously, the Cu interlayer is peeled off and lifted up by Li pillars. Furthermore, several hundred nanometer-sized Li whiskers are also observed. After the end of Li plating (EoLP), nucleation sites of metal Li pillar/whiskers are randomly distributed (i.e., no preference caused by an electrical field concentration owing to the surface roughness such as scratch lines on LLZO and Cu), and no surface changes are observed at other sites. During subsequent Li stripping, the heights of Li pillars decrease without substantial changes in the pillar diameter. After the end of Li stripping (EoLS), the coulombic efficiency is only approximately 20%, and numerous irreversible Li pillars/whiskers are still present as dead Li. These changes can be noticed in the focused ion beam (FIB) cross-sectional SEM image in Fig. 1b and Supplementary Fig. 4a. Large voids are observed at the LLZO/Li pillar interface. The generation of these voids can be attributed to sluggish Li diffusion and explained as follows³²: Li atoms at the LLZO/Li pillar interface are oxidized to Li^+ , and Li^+ rapidly moves toward LLZO. However, when the self-diffusion rate of Li atoms is rather slower than their oxidation rate, the structurally empty spaces in Li pillars are not immediately filled with the self-diffused Li atoms; consequently, as Li stripping proceeds, the contact between the Li

pillars and LLZO is gradually lost, which leads to the termination of Li stripping owing to an increase in resistance. Thus, the Li pillars are permanently retained as dead Li, causing capacity loss.

The other metal interlayer cells, which exhibited higher coulombic efficiency than the Cu interlayer cells and formed alloys with Li, showed different morphological changes than the Cu interlayer cells. The morphological changes of the Au interlayer cell can be described as follows (Fig. 1c and Supplementary Movie 3): During the initial Li plating, the morphology of the Au interlayer cell gradually swells, possibly owing to the alloying reaction accompanied by a volume expansion. With the continuation of Li plating, the sizes of the swollen regions increase to various micrometers, and thereafter, ball-ups are noticed in the swollen regions as if these regions are lifted by something with sizes of several tens of micrometers from below. However, some scratch lines still remain until EoLP, and additional surface morphological changes, including protruding Li whiskers and pillars, are not observed. In the subsequent Li stripping, although the ball-ups gradually shrink, they do not return to the pristine state, even at EoLS. As shown in the FIB cross-sectional SEM image obtained for EoLS (Fig. 1c), the Au interlayer is delaminated from LLZO, and it appears horizontally divided into two layers (whiter and darker gray). These layers are identified to be Li-Au alloy and Li, subsequently analyzed by *operando* XPS (details are provided in the next section). As Au produces the Li-Au alloy, in contrast with Cu, the Li-Au interlayer has high Li diffusivity and good electronic conductivity; thus, Li plating is expected to occur not only between the Li-Au alloy interlayer and LLZO but also on the surface of the interlayer. However, the FIB cross-sectional SEM indicates that Li plating occurs under the Li-Au alloy

layer, thus delaminating the Au (Li-Au alloy) interlayer at EoLP (Supp.). Thus, after Li stripping, the gaps induced by ball-ups have not fully recovered, and the coulombic efficiency is only ~55% which is higher than that of the Cu interlayer cell (20%) but less than those of the Zn (76%) and Ag (86%) cells.

However, in the cases of Ag and Zn interlayer cells, no ball-ups are detected, and the interlayer/LLZO interfaces are appropriately maintained. Moreover, these interlayer cells demonstrate higher coulombic efficiencies. For the Ag interlayer cell (Fig. 1d and Supplementary Movie 4), the entire interlayer initially begins to swell, and eventually, the scratch lines disappear. This suggests that the Li diffuses to the top surface and produces the Li-Ag alloy as a consequence of further lithiation. With the continuation of Li plating, the formation and growth of Li clusters, which exhibit irregular shapes (neither pillars nor whiskers with large aspect ratios), are uniformly noticed over the entire surface area. Simultaneously, Li whiskers develop locally, which grow to sizes of several hundred nanometers. Nevertheless, the Li whiskers grow laterally along the surface instead of perpendicular to the surface. As an exception, as observed in the upper right corner of Fig. 1d, Li columns with diameters and heights of a few tens of micrometers form and grow vertically. The growth of this columnar Li is believed to have been caused by the concentration of the electric field where the Ag is deposited in the morphological defect area of the LLZO. During successive Li stripping, the sizes of the Li clusters/whiskers considerably decrease, these clusters/whiskers shrink, and the proportion of Li remaining on the surface is much smaller than those in the cases of other metal interlayer cells. Cross-sectional FIB SEM images acquired for EoS (Fig. 1d) reveal that the Ag interlayer is thicker than that in the pristine state owing to volume expansion caused by alloying; nevertheless, the whole lithiated Ag interlayer appears to be uniformly alloyed and retains close interfacial contact with LLZO. Thus, from a morphological viewpoint, the Ag interlayer would be advantageous for stable Li plating/stripping, resulting in outstanding coulombic efficiency. Additionally, the Li on the lithiated Ag interlayer is uniformly deposited like a thin film, despite some increase in surface roughness.

In the case of the Zn interlayer cell (Fig. 1e and Supplementary Movie 5), the generation and growth of Li whiskers are mainly observed, but a small amount of Li clusters are also formed, similar to the case of the Ag interlayer cell, during Li plating; however, the sizes of Li clusters decrease during Li stripping, whereas those of Li whiskers do not substantially change, and Li whiskers remain on the interlayer surface at EoS. The microstructure of the lithiated Zn interlayer appears to be inhomogeneously alloyed (Fig. 1e). Similar to the cases of the Cu interlayer cell and bare LLZO surface, vertically grown Li whiskers with high aspect ratios are retained as dead Li owing to void production induced by the sluggish Li diffusion; nevertheless, Li clusters, which are formed on the lithiated Zn interlayer surface, can be reversibly stripped. To briefly summarize the *operando* SEM results, the morphologies and plating locations of Li deposits are discovered to be very closely correlated with the cell performance during stable Li plating/stripping.

The chemical and electronic structure changes during Li plating/stripping were analyzed by *operando* XPS without air exposure using an airtight transfer vessel and a modified sample holder that enabled cell cycling (Fig. 2 and Supplementary Fig. 2). According to the XPS spectra, the chemical states of natively oxidized Li compounds (such as LiO_x , LiOH , and Li_2CO_3) appearing at ~57 eV remains the same, regardless of the type of metal interlayer components. By contrast, the Li^0 state at ~55 eV corresponding to a metal or Li-metal alloy varies with the metal interlayer and their corresponding chemical states (including Au 4f, Ag 3d, and Zn 2p3). During Li plating, the metal content decreases with an increase in the proportion of Li on the outermost surface, and the opposite occurs during Li stripping. By correlating the electronic structure changes indicated by *operando* XPS results (~5 nm

information depth)³³ with the morphological changes revealed by *operando* SEM, the generation of a Li-Au alloy is expected; however, Li plating takes place beneath the Au (Li-Au alloy) interlayer, causing asymmetric chemical changes (Fig. 2b). During subsequent cycling, less changes occur in the composition of the Li-Au alloy. Chemical compositions of Li-Au alloys are approximately 1:1 Li:Au because of no surface plating of Li.

In the cases of the Ag and Zn interlayer cells, Li plating/stripping reversibly takes place on the interlayer surfaces such that the changes in the contents of Li and metals (determined from the XPS spectra) are symmetrical over multiple Li plating/stripping cycles. These findings are supported by the relatively higher coulombic efficiencies of the Ag and Zn interlayer cells than those of the Au cells. For the Ag interlayer cell, SEM indicates reversible changes in Li-Ag alloying/dealloying and Li cluster growth/shrinkage on the interlayer surface, and these changes in surface morphology are completely reflected by the changes in the chemical state of Li^0 , determined via XPS (Fig. 2c). In contrast, as indicated by *operando* SEM, Li whiskers in the Zn interlayer cell initially form and begin growing in the early stages of Li plating, ultimately enveloping the entire area of the interlayer surface. This phenomenon results in the predominant quantity of Li^0 measured by XPS at EoLP, as illustrated in Fig. 2d. Additionally, the chemical composition of Li/Ag is observed to be constant at each EoLP and EoS throughout repeated cycling, whereas the proportion of Li in the Zn interlayer cell continuously increases at EoLP with repeated cycling due to dead Li, reaching almost 100% after eight cycles. These results imply that the Ag interlayer cell leaves a smaller amount of dead Li after Li stripping than the Zn interlayer cell, leading to higher coulombic efficiency. The valence XPS spectra indicate the electronic structure at the LLZO/Li-metal alloy interface. (Supplementary Fig. 5). In the Au interlayer cell, Li plating/stripping primarily occurs at the LLZO/Au interlayer interface, causing irreversible changes in the valence spectra. However, in the cases of the Ag and Zn interlayer cells, the configurational changes in the valence spectra are discovered to be reversible owing to alloying/dealloying, as evidenced by changes in the Li content at the Li-metal alloy and LLZO interface. The time period during which the changes in the valence structure occur is longer in the case of the Ag interlayer cell than that in the case of the Zn interlayer cell. Thus, these observations support the conclusion that the Ag interlayer forms an alloy with a higher Li content.

Correlating the *operando* SEM and XPS reveals that the Ag interlayer cell has microstructural advantages in ensuring stable Li plating and stripping. However, the cells for *operando* analysis do not accurately represent a real cell packaged as a coin or pouch cell under stacking pressure. Thus, a *post-mortem* analysis was carried out on coin cells, which consisted of Cu foil as the current collector on top of the Ag interlayer and were assembled into a 2032 coin cell, to confirm the representativeness of the *operando* cells. The electrochemical performances of the cells used for *operando* experiments (SEM, XPS, and XRD) were consistent with those of the coin cell (Supplementary Fig. 6). Each Li plating/stripping state was chosen as the midpoint between the voltage plateaus that reflect the transitions of Li-Ag alloys on the charge/discharge profile (Fig. 3a). As shown in Fig. 3b, the morphological evolution at all Li plating/stripping states is in suitable agreement with the *operando* SEM results (Supplementary Fig. 7). Therefore, the *operando* experiments are believed to reliably represent the electrochemical reactions taking place during actual battery operation in this study. The microstructural evolution in the cross-section is depicted in the Fig. 3b–e. Note that in Fig. 3c, the layer labeled “re-deposits” is LLZO and Ag that was inevitably sputtered during the cross-sectional Ar^+ polishing process. However, these re-deposits can be distinguished from Li deposits by backscattered electron (BSE) images and an X-ray energy dispersive spectroscopy (XEDS) elemental distribution analysis (Supplementary Fig. 8). From the pristine state to state III of Li plating (Li_xAg , $x < 3$), the thickness of

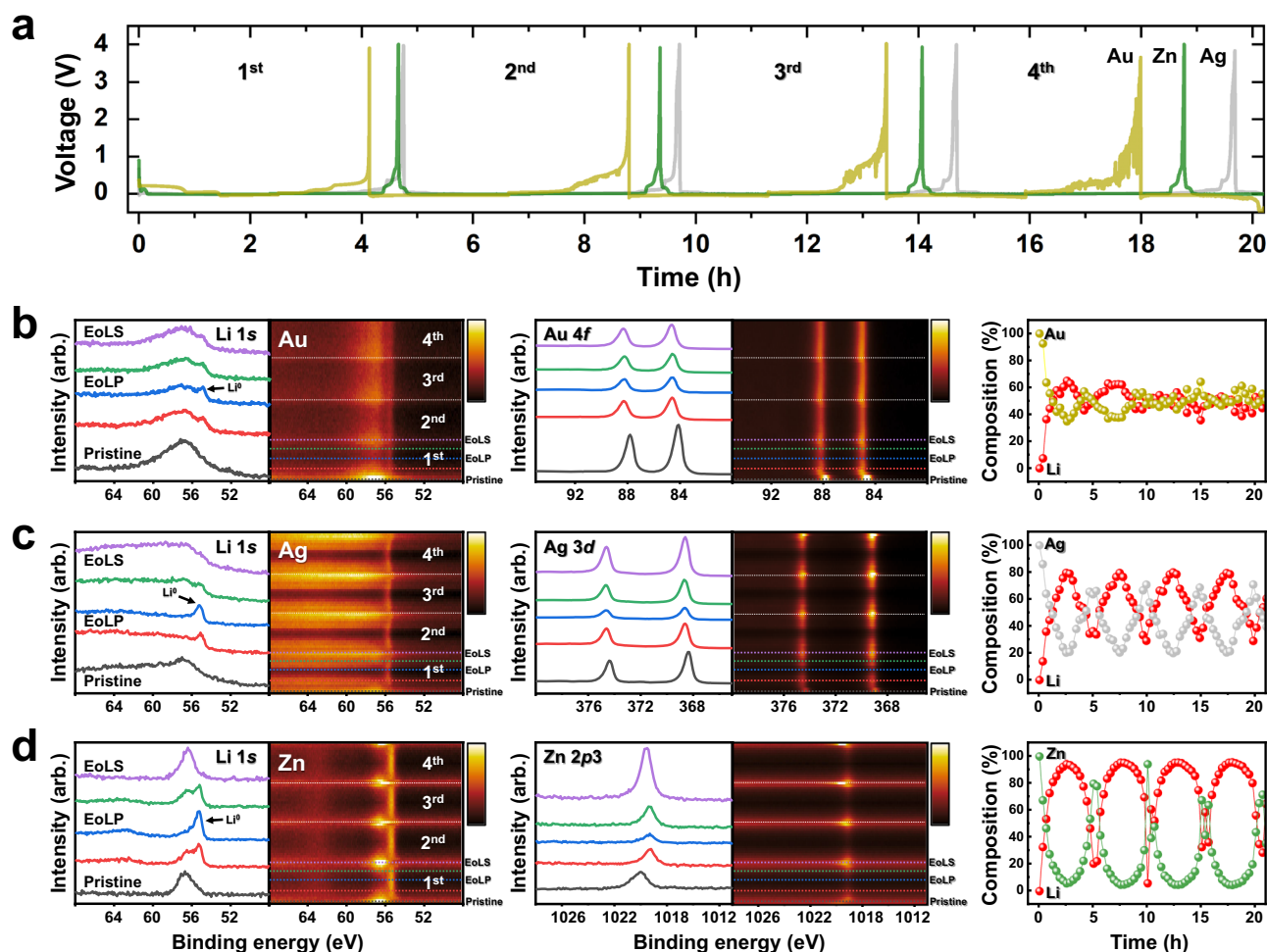


Fig. 2 | Operando XPS of metal|LLZO|Li cells. a Charge/discharge profiles and corresponding XPS spectrum according to the Li plating/stripping states during the first cycle and spectra from four cycles along with their composition profiles; **b** Li 1s

with Au 4f, **c** Li 1s with Ag 3d, and **d** Li 1s with Zn 2p3. Red and green profiles correspond to the intermediate states between the pristine state and EoLP and EoLS.

the Ag interlayer increases from 200 to 1000 nm, which is attributed to the volume expansion caused by Li-Ag alloying, which appropriately matches with the voltage plateaus in the charge/discharge profiles. After state II, Li clusters are observed on the lithiated Ag (denoted as Li-Ag alloy) interlayer, and after further lithiation, Li clusters grow and merge into the thin-film morphology with some roughness. In the subsequent Li stripping, the sizes of Li clusters initially decrease, and then, the Li-Ag alloy layer becomes thinner in the reverse order of Li plating. Note that the Li-Ag alloy interlayer/LLZO interface remains unchanged during all Li plating/stripping states. Therefore, the Li-Ag alloy plays an important role as a buffer layer to maintain an appropriate interface for the transport of Li atoms from the Li clusters to LLZO and vice versa. Thus, uniform and reversible Li plating/stripping and good coulombic efficiency can be achieved in the Ag interlayer cell.

Electrochemical performances

To further validate the efficacy of uniform Li plating/stripping according to the location of Li plating (on the surface or at the interface), which represents the situation in a real cell with the stacking pressure, the electrochemical test of Ag and Au interlayers were conducted in coin cells (Fig. 4). A half-cell, comprising a 200-nm-thick Ag interlayer deposited on one side of LLZO and 40- μm -thick Li foil pressed on the opposite side of LLZO, was assembled and examined at 25 °C. Figure 4a shows the cycling performance of the Ag interlayer

half-cell during repeated Li plating/stripping, and the cell demonstrates exceptional stability, maintaining stable performance over 962 cycles. In contrast, the Au interlayer full-cell, which exhibits Li plating beneath the Au interlayer with a less uniform distribution than that in the case of the Ag interlayer half-cell, experiences a short circuit after five cycles (Supplementary Fig. 9). Considering the superior performances of the Ag interlayer cells, we expected that Ag interlayer could potentially serve as a suitable interlayer for anode-less batteries. To establish this, electrochemical tests were performed on hybrid solid-state full-cells. These cells incorporated a $\text{LiNi}_{1/3}\text{Co}_{1/3}\text{Mn}_{1/3}\text{O}_2$ (NCM111) cathode wetted with an ionic liquid (i.e., 2 M lithium bis(fluorosulfonyl) imide (LiFSI) in N-methyl-N-propyl pyrrolidinium bis(fluorosulfonyl) imide (Pyr13FSI)) and a 100-nm-thick Ag interlayer at the solid electrolyte/current collector interface for the anode. The cell was operated at different current densities from 0.1 to 1.0 mA cm^{-2} with 0.1 mA cm^{-2} step and cycled five times at each current density at 25 °C (Fig. 4b). Although these values may not meet practical battery demands, the Ag interlayer full-cell consistently demonstrates superior performance when compared with the Au interlayer full-cell. Moreover, the Ag interlayer full-cell operates at current densities up to 0.9 mA cm^{-2} (Fig. 4c), a value comparable to the highest current density of 0.8 mA cm^{-2} observed when testing the Ag interlayer half-cell (Supplementary Fig. 10). In contrast, the Au interlayer full-cell short circuits at 0.3 mA cm^{-2} (Supplementary Fig. 9). These consistent and excellent electrochemical test results for the Ag interlayer cell imply that

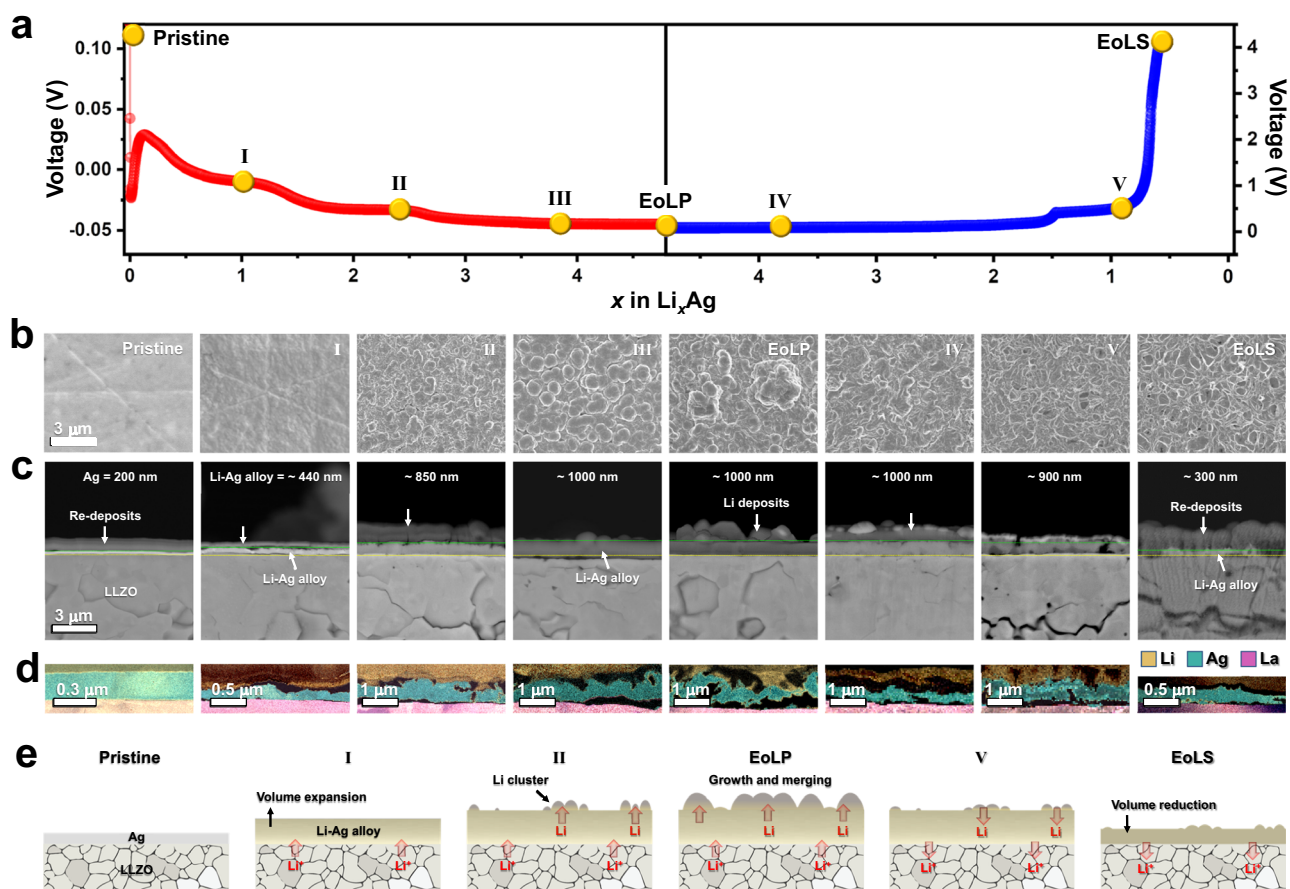


Fig. 3 | Microstructural evolution determined via *post-mortem* analysis of the Ag|LLZO|Li cell. **a** Charge/discharge profiles (Li content x in Li_xAg) and corresponding *post-mortem* **(b)** surface and **(c)** cross-sectional SEM images with **(d)** STEM-EELS spectrum image maps (Li: Red, Ag: Green, and La: Blue). **e** Schematics

depicting the microstructural evolution during Li plating/stripping. Note that the same scale bars are used in all images in **(b-c)**, whereas different scale bars are employed for each image in **(d)**.

uniform Li plating onto the Ag interlayer play a critical role as an interface control buffer layer to mitigate short circuit failure. Therefore, it is imperative to comprehensively elucidate the corresponding mechanism.

Stable Li plating mechanism

Previous experimental results reveal that Li plating/stripping on the surface passing through the Li-Ag alloy plays an important role in maintaining the Ag interlayer/LLZO interface for stable cell operation in an AL-SS-LMB. However, the mechanism of Li plating passing through the interlayer cannot be adequately explained by conventional diffusion theory and the nucleation and growth model. At the interface between the Li-Ag alloy and LLZO, the concentration of Li is highest, and it decreases toward the surface; thus, it is reasonable to expect Li to be plated at the interface, regardless of the type of metals. Thus, these phenomena are not sufficient to explain the Li plating at the Li-Au/LLZO interface, suggesting that a difference in these two interfaces plays a role. Notably, the wettability of the Li-Au alloy on LLZO is better than that of the Li-Ag alloy^{34–36}, suggesting that the adhesion energy between the Li-metal alloy and LLZO may determine the location of the Li plating. In addition, even if Li diffusion is fast enough to provide a sufficient Li concentration on the surface for nucleation, this also fails to elucidate the occurrence of Li plating at the Li-Au/LLZO interface because the Li diffusivity in Au is higher than that in Ag (Supplementary Fig. 11). In the cases of the thick Li-Ag alloy anode (active Li reservoir)^{29,30} and various thin metal substrates for LIBs³⁷, the mechanisms of stable cell cycling have been suggested by explaining Li

plating/stripping based on alloying/dealloying and solid solution depending on the phase diagram. Nevertheless, this mechanism, which implies that Li is deposited in the direction toward the liquid electrolyte rather than toward the current collector, does not fully account for the Li plating behavior on the surface passing through the Ag interlayer in solid electrolytes. Thus, the mechanism of Li plating in the Ag interlayer cell is likely to be closely related to not only the production of alloys and their Li solubilities but also the microstructures of the alloys as the Li-Ag alloy provides a pathway for Li diffusion.

To determine the Li-Ag alloying/dealloying mechanism during Li plating and stripping, an *operando* XRD experiment was conducted (Fig. 5). The charge/discharge profiles obtained during *operando* XRD are in suitable agreement with the *operando* SEM and XPS results. The Ag interlayer cell dynamically demonstrates the continuous formation and phase transformation of Li-Ag alloys and reversible changes between Li plating and stripping during five cycles (Fig. 5 and Supplementary Fig. 12). Notably, the Li-Ag alloy phases are identified to be not only all stable Li-Ag alloy phases (namely, β (LiAg), γ_3 (Li_9Ag_4), γ_2 ($\text{Li}_{10}\text{Ag}_3$), and γ_1 (Li_{12}Ag)) in the phase diagram at room temperature, but also Li_3Ag (Supplementary Figs. 13,14 and Supplementary Table 1). However, in the Zn interlayer cell, only the LiZn phase is reversibly produced, and it disappears near EoLS, without any intermediate Li_xZn alloys ($x < 1$, Li_2Zn_3 , LiZn_2 , Li_2Zn_5) (Supplementary Fig. 15). For the Au interlayer cell, the phase transformation of the Li-Au alloys occurred irreversibly, regardless of Li plating/stripping (Supplementary Fig. 16). This inconsistent phase transformation is believed to be due to the Li plating under the Li-Au alloy interlayer causing the deamination of the

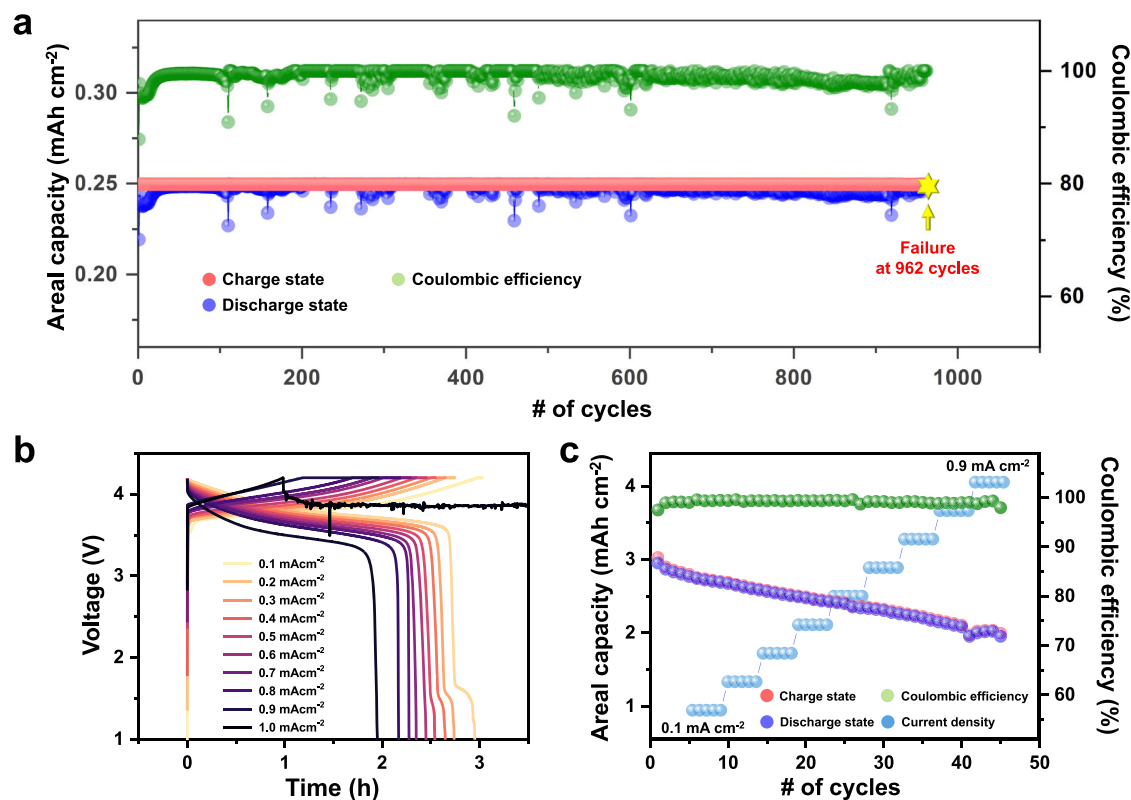


Fig. 4 | Electrochemical performances. **a** Co-plot of areal capacity and coulombic efficiency vs. cycling of the Ag|LLZO|Li half-cell. **b** Charge/discharge profiles and **(c)** co-plot of areal capacity and coulombic efficiency vs. cycling of the Ag|LLZO|NCM

full-cell at different current densities. The cell failed during the early stages of discharge at 0.9 mA cm⁻².

Li-Au alloy interlayer from the LLZO, resulting in poor the interfacial contact and hence the inhomogeneous lithiation/delithiation. The phase of Li-Ag alloys sequentially transform in the order β , γ_3 , γ_2 , Li_3Ag , and γ_1 , appropriately matching the voltage plateaus in the charge/discharge profile shown in Fig. 5c and the differential capacity versus voltage (dQ/dV) curves (Supplementary Fig. 17)³⁸. Generally, the transformation toward the Li-Ag alloy phase with higher Li content is expected to occur by a continuous supply of Li during the charging. However, the transformation of Li_3Ag from γ_2 ($\text{Li}_{10}\text{Ag}_3$) takes place in the decreasing order of Li content (Li_xAg , x is decreased from 10 to 9). In other words, in reverse order of Li content, the γ_2 was observed first and Li_3Ag later. The formation of Li_3Ag , which is not a stable alloy phase shown in the phase diagram, has been reported during the electrochemical delithiation in the Li-Ag alloy anode^{29,30,39}.

To validate the effect of phase transformation kinetics on Li-Ag alloy generation, additional *operando* XRD experiments were conducted. To determine if any Li-Ag alloy phase was missed due to the low acquisition speed of XRD, the acquisition speed was increased from 30 to 5 min by confining only in the 2θ range of 30–42°, where all Li-Ag alloy phases can be identified; nevertheless, the same phase transformation, including the formation of Li_3Ag , of Li-Ag alloys was observed (Supplementary Fig. 18). Furthermore, the reaction kinetics were varied to examine the changes in the phase transformation behavior. The charge rate for each cycle was continuously increased to 0.01, 0.05, 0.1, and 0.2 mA cm⁻² at the same areal capacity (Supplementary Fig. 19). No γ_1 was detected during the first Li plating cycle, and the same Li-Ag phases, such as γ_1 and Li_3Ag , were observed in the following cycle. The reason for the absence of γ_1 is the lack of Li because phase transformation to β is suggested to more preferably occur during the slower reaction kinetics because of a more uniform reaction in the Ag interlayer. (At the current densities of 0.01 and

0.05 mA cm⁻², the areal capacities at the maximum intensity of β are 0.07 and 0.05 mA cm⁻², respectively.) Therefore, Li_3Ag has been verified to usually produce by lithiation via an electrochemical reaction.

To further understand the phase evolution during Li-Ag alloying, first-principles calculations were performed to evaluate the convex hull of the Li-Ag binary system (Supplementary Fig. 20). As experimentally identified, the formation of β (LiAg) followed by the evolution of γ_3 (Li_9Ag_4) during lithiation was predicted. In more Li-rich compositions, Li_3Ag was discovered to lie on the hull, and γ_2 and γ_1 were estimated to be metastable with above-hull energies of 15 and 11 meV/atom, respectively⁴⁰. Note that the contribution of configuration entropy is not included in Supplementary Fig. 20; therefore, γ_2 and γ_1 can be more stable at room temperature. According to the Li contents in Li-Ag alloys, Li_3Ag ($x = 0.75$ in $\text{Li}_x\text{Ag}_{1-x}$) should generate before γ_2 ($x = 0.77$ in $\text{Li}_x\text{Ag}_{1-x}$) during lithiation; however, γ_2 was detected before Li_3Ag (Fig. 5). This behavior can be comprehended in terms of phase transformation kinetics. As Li_3Ag and γ -brass-type phases exhibit different crystal structures and local symmetries (Supplementary Fig. 21), evolution of γ_3 into γ_2 without major crystal structure change would be kinetically more favorable than that into Li_3Ag ⁴¹. With the progress of lithiation, metastable γ_2 starts to separate into Li_3Ag and metal Li phase, which is a thermodynamically more stable state. This kinetic pathway of phase transformation adequately corresponds with the experimental observation, where phase evolution during the lithiation of Ag followed the order β , γ_3 , γ_2 , Li_3Ag , and γ_1 .

For investigating the microstructures and phase separation of Li-Ag alloy, particularly for Li_3Ag , cryo-TEM was conducted (Fig. 6a–d). The Li alloy and its compounds are susceptible to degradation because they easily react with oxygen and moisture in air and to delithiation and structural changes induced by Ga⁺ during FIB processing and the *e*-beam during TEM (Supplementary Fig. 22), TEM specimens were

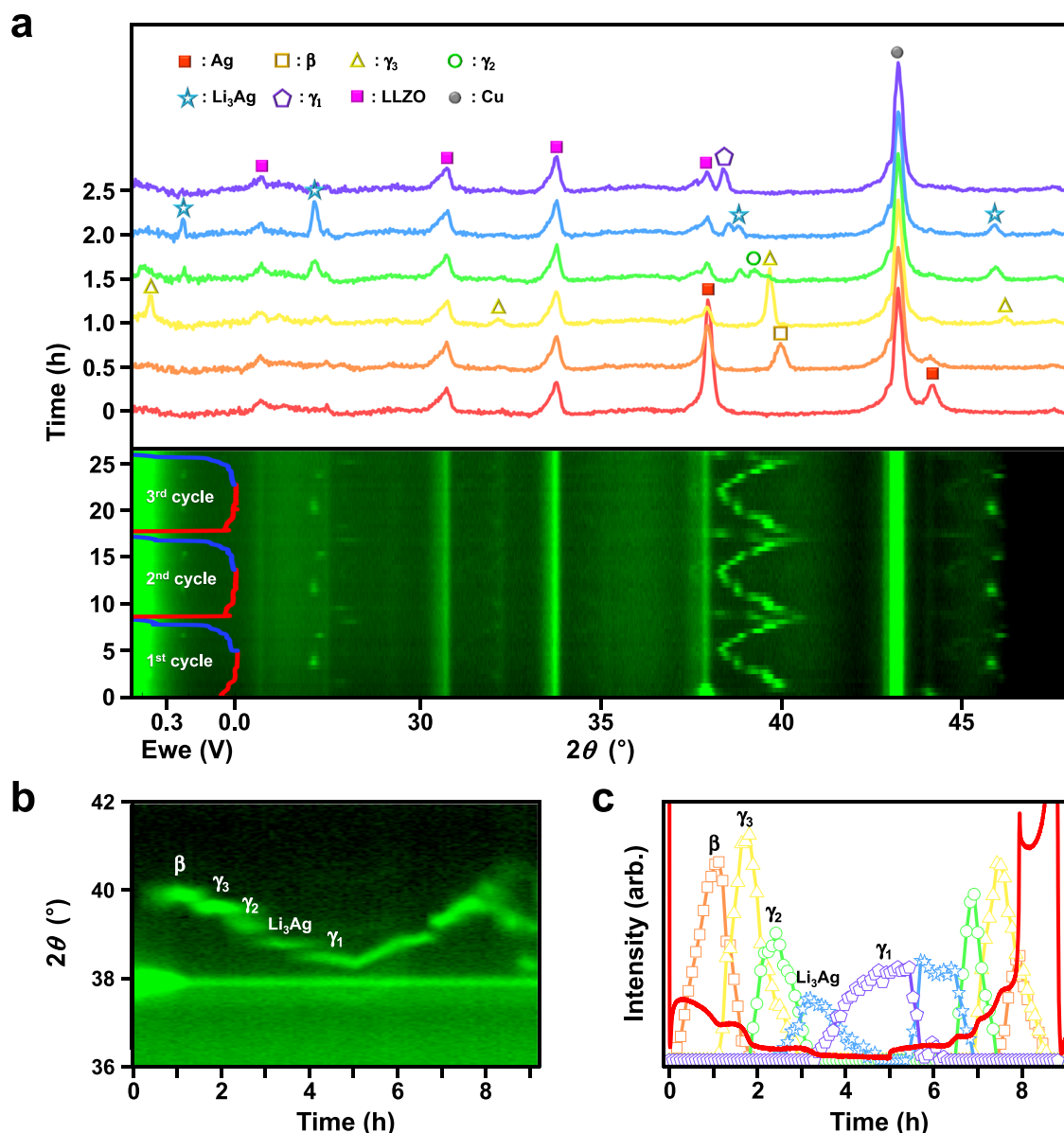


Fig. 5 | Operando XRD of the Ag/LLZO/Li cell. a Operando XRD patterns and pattern image acquired at 2θ of $10\text{--}60^\circ$ at 30 min/spectra during the first three cycles. Inset shows the charge/discharge profile. **b** Operando XRD pattern image

obtained at 2θ of $36\text{--}42^\circ$ at 5 min/spectra during one cycle. **c** Intensity profiles of the indexed phase of the Li-Ag alloy with the charge/discharge profile.

carefully prepared using an airtight transfer vessel and cryo-FIB to minimize the impacts on the surfaces and microstructures of these materials (Supplementary Fig. 23). As shown in the high-angle annular dark-field scanning transmission electron microscopy (HAADF-STEM) image in Fig. 6a, nanosized Li-Ag alloy particles are noticed in plated Li and lithiated Ag interlayer on LLZO, which are determined as Li_3Ag and γ -brass-type phases (γ_3 , γ_2 , and γ_1), respectively. Detailed microstructure of Li_3Ag is observed in the state III of Li plating, where Li_3Ag and γ -brass-type phases coexist, attributed to phase separation during previous operando XRD. Li-Ag nanoparticles, which are identified as Li_3Ag by selected area diffraction pattern (SADP), appear to be intermixed in the plated Li matrix in Fig. 6b and d. This microstructure is very similar to the microstructure typically produced by spinodal decomposition owing to phase separation⁴², which can be speculated to have occurred during the transformation of γ_2 into Li_3Ag in previous operando XRD.

To further confirm that the abovementioned microstructure originated from phase separation, a thinner Ag interlayer (thickness:

30 nm) was lithiated to examine the phase-separated microstructure throughout the layer. As depicted in Fig. 6c and Supplementary Fig. 24, the outline of the Ag interlayer can be traced, and a phase-separated microstructure is noticed in the Ag interlayer. Therefore, the phase-separated microstructures of nanosized Li_3Ag particles embedded in the Li matrix stem from the transition of γ_2 to Li_3Ag and Li, as revealed by operando XRD. This two-phase-separated microstructure resulting from spinodal decomposition during electrochemical lithiation has also been reported for olivine LiMPO_4 ($M = \text{Fe}$ and Mn) and spinel $\text{Li}_4\text{Ti}_5\text{O}_{12}$ ^{42–45}. The mechanism of spinodal decomposition is as follows: a single phase, whose composition lies in the thermodynamically unstable region of the phase diagram, spontaneously separates into two phases (without nucleation) due to composition fluctuations⁴⁶. During Li-Ag alloying by an electrochemical reaction, the phase separation of metastable γ_2 would be triggered by composition fluctuations caused by the continuous supply of Li atoms. Although the phase separation does not fully satisfy the compositional requirements of spinodal decomposition

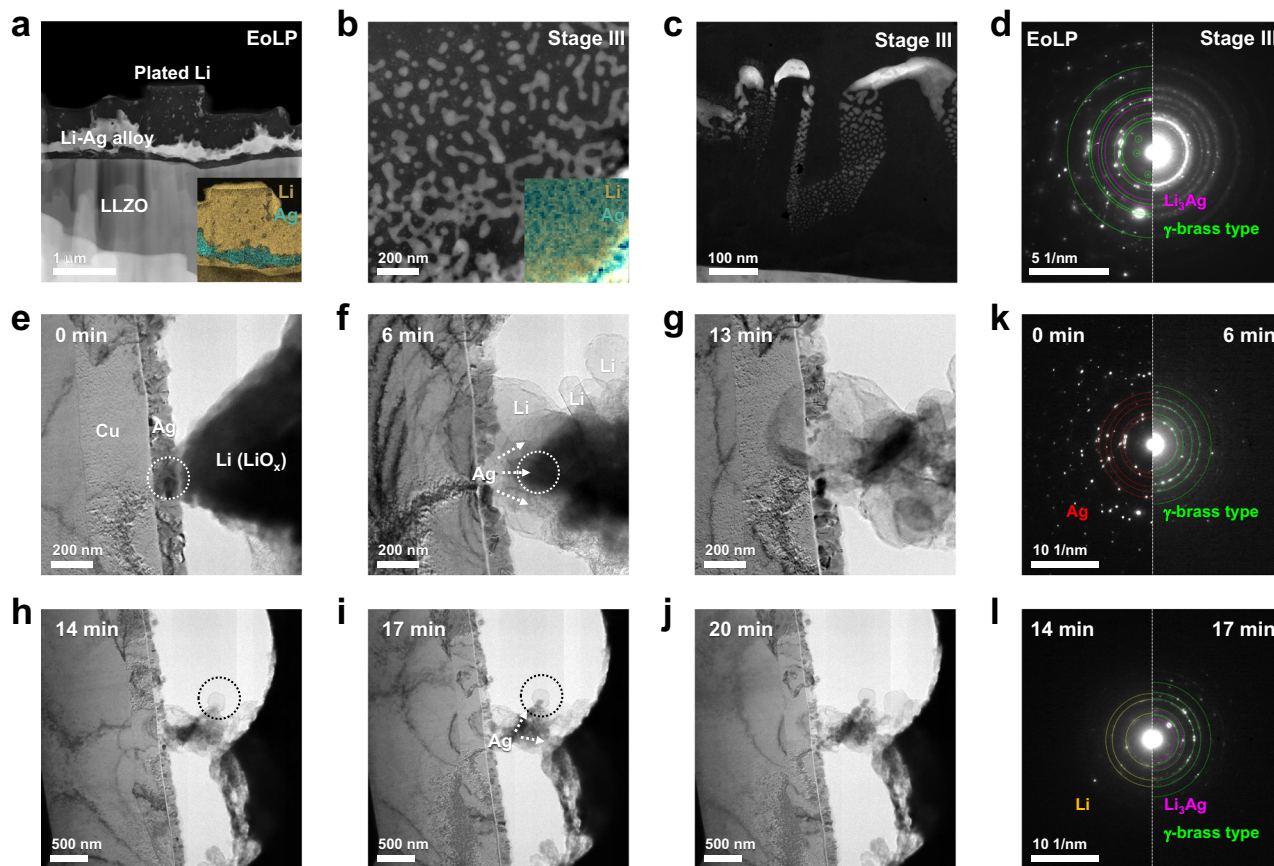


Fig. 6 | Microstructure of the Li-Ag alloy. HAADF-STEM images and corresponding overlaid EELS-SI elemental maps of Li and Ag (inset) of a 200-nm-thick Ag|LLZO|Li cell at (a) EoLP and (b) state III. c HAADF-STEM image of a 30-nm-thick Ag|LLZO|Li cell at state III. d SADPs acquired for the Li-Ag alloy region in (a) (left half)

and nanosized Li-Ag alloy grain region in (b) (right half). **In-situ TEM.** e–j Still-cut TEM images and corresponding SADPs (k and l) obtained from the dotted circle area in (e and f) and (h and j), respectively.

because of the inflow and outflow of Li during the electrochemical reaction, it is suggested that these processes are similar, as are the resulting phase-separated microstructures.

Thus, the mechanism of Li plating in metal interlayer cells can be proposed as follows. At the metal interlayer/LLZO interface, the reduced Li atoms diffuse into the metal interlayer and form a solid solution. In the case of the Au interlayer cell, due to the narrow solid-solution region with Li and different crystal structures of Li-Au alloys, phase transformation to a Li-rich alloy cannot be achieved. In addition, when Li is continuously supplied above the limit of Li solubility in the intermetallic alloy, Li atoms can no longer diffuse into the Li-metal alloy and are plated at the Li-Au alloy/LLZO interface^{29,30}. Nevertheless, Li-Ag alloys demonstrate wide solid-solution regions and similar crystal structures of γ -brass-type phases, leading to the formation of Li-rich alloys. Additionally, phase separation to Li_3Ag and Li, which provide the growth sites for Li, occurs without the thermodynamic energy barrier for nucleation. Moreover, as phase separation simultaneously takes place in the microstructure of the entire Li-Ag alloy, Li can be plated both at the Li-Ag alloy/LLZO interface and on the surface. In the case of the *operando* cell, Li plating would have been occurred more easily on the open surface than at the Li-Ag alloy/LLZO interface, which was in close contact. However, coin cells contain no open surfaces where Li can grow because the current collector is packaged under stacking pressure; thus, Li plating preferentially occurs on the side of the interlayer with lower wettability (lower adhesion energy), i.e., at the Li-Ag alloy/LLZO interface and/or the Li-Ag alloy/Cu current collector interface. According to the experimental results from the coin cell, the Li-Ag alloy has good wettability to LLZO^{35,36}, whereas Li wettability on

Cu is poor because Cu is lithiophobic. This difference in wettability probably caused the Li plating to occur at the less intimate interface between the Li-Ag alloy interlayer and the Cu current collector.

Inhibiting the dendritic growth of Li deposits

Upon Li stripping, more dead Li remains in the Zn and Cu interlayer cells due to the Li pillar/whisker morphology with a large aspect ratio, which is preferentially grown in the crystal orientation owing to its crystallographic nature⁴⁷. Nevertheless, for the Ag interlayer cell, the Li clusters grow without preferential orientation. The formation of these dendritic Li deposits with high aspect ratios results in inferior coulombic efficiency due to void formation owing to sluggish Li diffusion and the loss of physical contact at the LLZO/Li deposits and Li deposit/current collector interface. Moreover, these deposits can also cause a short circuit in LLZO due to uneven current distribution. The morphologies and preferred orientation growths of Li deposits may depend on the adsorption of impurities, type of liquid electrolyte, electrodes as deposition substrates, and charging conditions in liquid-electrolyte-based batteries^{48–52}. As all other conditions are the same, the metal adsorbed as an impurity on Li deposits is considered the major controlling parameter in determining the morphology of Li in this study.

According to the compositional results of the XPS analysis (Supplementary Fig. 5), for the Zn interlayer cell, the content of Li on the surface is almost 97% at EoLP and increases up to 99% after eight cycles. This indicates that the chemical composition of the Li whisker is close to that of pure Li. However, for the Ag interlayer cell, even if the surface is almost covered by Li deposits owing to the merging of the

growing Li clusters during repeated cycling, as shown in cross-sectional SEM images, the content of Ag in Li deposits on the surface is still more than 20% at EoLP. This indicates that the Li deposits contain a large amount of Ag (solid solution of δ -Li). Such Ag-dissolved Li deposits noticed in AL-SS-LMBs have also been reported in other studies^{22,53}. According to the binary phase diagrams of Ag and Li (Supplementary Fig. 14), the solubility of Ag in Li is relatively high (of the order of a few atomic percent), whereas those of Zn and Au are less than approximately 0.5 at.% at room temperature. Furthermore, Ag exhibits substantially high solubility in Li, which enables the production of solid solutions by the interdiffusion of Li and Ag and even alloy phases at room temperature. The spontaneous reaction between Ag nanoparticles and Li metal upon physical contact was experimentally confirmed only via SEM (Supplementary Fig. 25 and Supplementary Movie 6). Dispersed Ag nanoparticles on the Li substrate are spontaneously swollen by lithiation and form an alloy. Finally, Li regrows via the Li-Ag alloys. In addition, the dissolution of Ag into Li by electrical bias was experimentally characterized using in-situ TEM. To that end, an FIB-prepared sample of a Ag thin film deposited on a Cu foil was mounted on a Cu grid as a fixed positive electrode, and a Li(LiO_x)-coated Pt/Ir tip, which could be manipulated for direct contact, was used as the negative electrode (Supplementary Fig. 26). After the Li(LiO_x)-coated tip came into contact with the Ag layer, an electrical bias of 2.0 V was applied. Dendritic Li nanocrystals, which originate from the reduction of LiO_x by electrical biasing, generate and grow around the apex of the tip (Fig. 6e–g and Supplementary Movie 7). Subsequently, the grain boundaries of the Ag thin film open up, and the grain size decreases, implying the migration of Ag atoms to Li. Dendritic Li nanocrystals with well-developed facets lose their original shapes because of the dissolution of Ag into Li, and upon additional biasing, massive clusters of Ag, as shown in the darker contrast marked by a dotted circle in Fig. 6h and i, diffuse through the Li nanocrystals and eventually form a Li-Ag alloy, identified by SADP (Fig. 6k–l and Supplementary Fig. 27). Therefore, during in-situ TEM, the electrical bias can cause Ag atoms to dissolve into the Li metal, and changes in the morphology of Li metal were experimentally confirmed.

In summary, via correlation analysis of multiple *operando/post-mortem* experiments, the morphological, chemical, and structural changes in AL-SS-LMBs with metal interlayers during Li plating/stripping were systematically investigated. The interlayer cells based on metals with low Li solubilities (including Cu) or inability to produce Li-rich alloys (Au and Zn) demonstrate Li plating at the metal interlayer/solid electrolyte interface, which implies loss of contact between the solid electrolyte and metal interlayer (or current collector); this leads to inferior discharge characteristics due to an increase in the proportion of dead Li. Nevertheless, in the case of the Ag interlayer cell, Li plating takes place on the surface passing through the lithiated Ag interlayer without the loss of the contact between the solid electrolyte and metal interlayer (or current collector). This is due to the formation of a Li-rich alloying phase, which favors Li growth on the Ag (Li-Ag alloy) interlayer surface. Particularly, the separation of Li₃Ag and Li may have resulted in the growth of Li deposits on the interlayer surface instead of at the interface. Moreover, metal Li deposits do not grow as dendrites with high aspect ratios and are plated as irregularly shaped Li clusters with large contact areas on the interlayer surface, decreasing the amount of dead Li during Li stripping and mitigating delamination of the current collector. This is because Li and Ag exhibit high chemical reactivities to each other, and thus, when metal Li deposits are generated and grow on the surface, Ag is dissolved, forming a solid solution, thus inhibiting dendritic growth. Overall, by exploring this interface control strategy by revealing the role of the metal interlayer, we aim herein to contribute to the ongoing efforts to overcome the challenges associated with AL-SS-LMBs and move closer to their widespread adoption in various applications.

Methods

Cell fabrication

The LLZO pellet, with a nominal composition of Li_{6.5}La₃Zr_{1.5}Ta_{0.5}O₁₂ (thickness: 500 μ m; diameters: 14 mm), was purchased from Toshiba Manufacturing Co., Ltd. The physical properties were characterized as shown in Supplementary Fig. 28. The ionic conductivity of LLZO pellet was measured by alternating current (AC) impedance measurements, and the pellet exhibited conductivities of 0.74, 1.71, and 2.72 mS cm⁻¹ at 25, 45 and 60 °C, respectively. The pellets were sequentially polished with P800-, 1200-, 2000, and 3000-grit sandpapers. The polished pellets were immersed in a 1 M HCl solution for 3 min followed by washing with ethanol to increase the interfacial affinity with the metal interlayer and Li metal by removal of Li₂CO₃ and LiOH^{54,55}. Thereafter, three types of cells, namely, *operando*, half, and hybrid full-cells, were fabricated using the polished LLZO pellets in a dry room, where the dew point was maintained below -50 °C. *Operando* cells (200-nm-thick metal|LLZO|Li cells), used to examine Li plating and stripping through metal interlayers via *operando* analyses, consisted of a Li metal electrode (20- μ m-thick Li metal on a 10- μ m-thick Cu foil (Honjo Metal Co., Ltd.) with a diameter of 12 mm) as the counter electrode and a thin metal layer (Ag, Zn, Au, or Cu) with a diameter of 12 mm as the working electrode. The working electrode was deposited on the polished side of the LLZO pellet masked with polyimide tape comprising a 12-mm-diameter hole using a radio frequency (RF) magnetron sputter. All metal interlayers were deposited under a base pressure of $\sim 10^{-7}$ Torr at a working pressure of 5×10^{-3} Torr under a 40-sccm flow of high-purity Ar gas (99.9999 %) at a constant substrate temperature of 22 °C. The purity of the metal targets was 99.99%, and pre-sputtering was conducted for 10 min. Then, the metal interlayers were sputtered to a target thickness of 200 nm at a RF power of 150 W (for Ag, the deposition rate was 10 nm/min). Connecting the sputtering system to an Ar-filled glove box enabled loading the LLZO pellets into the sputtering chamber without air exposure. After metal deposition, all the samples were vacuum-sealed in an Ar-filled glovebox and taken to a dry room for cell fabrication. A Li metal electrode (40- μ m-thick Li metal on a 10- μ m-thick Cu foil (Honjo Metal Co., Ltd.) with a diameter of 12 mm) as the counter electrode was pressed on the unpolished side of the LLZO pellet by applying a pressure of 250 MPa for 3 min using a cold isostatic press. This assembly was employed as the cell in each *operando* analysis.

To construct the half-cells, a 10- μ m-thick Cu foil current collector was placed on the working electrode side (i.e., in contact with the thin metal interlayer) of the metal|LLZO|Li foil assembly, and 2032 coin cells were assembled. To fabricate hybrid full-cells, an anode (a thin layer of metal) was made using the same method as the *operando* half-cell. NCM111 (loading capacity: 3.2 mAh/cm², diameter: 4 mm, Samsung SDI) coated on Al was used as the cathode, and a catholyte, 2 M LiFSI in NPyr13FSI (Kanto Chemical Co., Inc.), was placed dropwise on the cathode and then infiltrated into the cathode under vacuum; the infiltrated amount of the ionic liquid was 20 wt% relative to the cathode weight. Thereafter, the infiltrated cathode was placed on the unpolished side of the LLZO pellet followed by assembly into a 2032 coin cell.

Electrochemical characterization

Charge/discharge characteristics of the hybrid full-cells were analyzed at 25 °C using a battery cycler (TOSCAT-3100, Toyo System). The cells were charged using a conventional constant current (CC)-constant voltage (CV) protocol and discharged in the CC mode over the potential range of 1–4.2 V (vs. Li⁺/Li). Electrochemical profiles at 25 °C were acquired by stepwise increasing the current density; that is, the cells were charged/discharged at current densities in the range from 0.1 to 1.0 mA/cm² and cycled five times at each current density. Critical current density measurements using half-cells were performed with Li plating current densities from 0.1 to 1.0 mA/cm² and a step size of

0.1 mA/cm² at a fixed Li plating capacity of 0.25 mAh/cm² at 25 °C. However, the Li stripping current density was fixed at 0.05 mA/cm², and the current was applied until the cell voltage reached 4 V. All cells were vacuum sealed and were performed the electrochemical tests in the temperature-controlled chamber without exposure to the atmosphere.

Operando analysis

Operando SEM was conducted in an E-SEM (Quanta650, FEI) operated at 2 kV to minimize the *e*-beam damages. Airtight transfer module (Kammrath & Weiss GmbH) was modified for electrochemical battery cell cycling via electrical feedthroughs to the outside of the SEM chamber. A half-cell battery (metal|LLZO|Li/Cu) was mounted on a homemade holder that could be separately connected to two electrodes. The bottom counter electrode (Li/Cu) was contacted with LLZO by placing it on the sample holder, and the upper working electrode was rigidly connected to LLZO by pressing it with a Cu tip. The same sample holder configuration was employed for subsequent *operando* XPS. *Operando* SEM images were acquired at 10-min intervals to prevent the *e*-beam effect, leading to an unintended surface reaction different from that of galvanic cycling. As a control experiment, the morphological changes induced by the *e*-beam alone without galvanic cycling were examined, as shown in Supplementary Fig. 29, and no morphological changes were observed, although hydrocarbon contamination appeared. This suggests that the *e*-beam exposure during SEM observations was not sufficient to induce electrochemical reactions, in contrast with galvanic cycling.

Operando XPS was performed using in-lab-based XPS equipment (Versaprobe I, ULVAC-PHI). XPS spectra (namely, O 1s, Li 1s, C 1s, Ag 3d, Zn 4f, and Au 4f spectra) were obtained at 20 min/cycle in real-time during actual operation. Using the airtight transfer vessel for XPS instrument, all battery cells assembled in the dry room were transferred from the glove box to the XPS chamber without additional exposure to the ambient atmosphere.

Operando XRD was conducted by modifying a 2032 coin cell. To perform cell cycling during XRD, a 10-mm-diameter hole for the X-ray beam path was drilled in the center of the upper half of the 2032 coin cell case, and after assembling the coin cell parts, the hole was sealed with polyimide film using an epoxy adhesive. *Operando* XRD was conducted using a Panalytical X'Pert Pro diffractometer with a Cu K α (λ = 1.54 Å) X-ray source. θ -2 θ scans were performed back-to-back during the charge/discharge cycles. Larger-range scans (2θ = 10–60°) were completed in 30 min, whereas shorter-range scans were accomplished in 5 min (2θ = 36–42°). Peak intensities were acquired by fitting the patterns obtained from the shorter-range scans with Gaussian functions on a quadratic background. The open circuit voltage of metal interlayer half-cells were typically measured between 2.5 and 2.7 V. To ensure that sufficient Li was stripped during the discharge process, the cut-off voltage was set to 4 V, a value that does not electrochemically degrade LLZO.

Electron microscopy

Cross-sectional samples of the *operando* SEM and *post-mortem* cells were prepared by FIB (Helios Nanolab 450FI, FEI) and a cross-section polisher (IB-19520CCP, JEOL) before being analyzed by SEM (SU 8030, Hitachi). TEM was conducted using a double Cs-corrected Titan cubed microscope (FEI) with a Quantum 966 energy filter (Gatan Inc.). For cryo-TEM, the cryo-FIB sample was prepared by Quanta-3D FIB using a cryo-transfer system (Alto 2500) while maintaining the temperature below −140 °C and examined using an airtight cryo-TEM holder (Mel-Build) at −120 °C. In-situ TEM was performed by a biasing manipulator TEM holder (Hummingbird Scientific). STEM-EELS was conducted using an electron beam current of 40 pA to minimize the knock-on damages. All samples were transferred between the glove box and analytical instruments without exposure to the atmosphere.

First-principles calculations

Density functional theory calculations were performed using Vienna ab initio simulation package (VASP)⁵⁶. We used PBEsol as an exchange-correlation functional⁵⁷, and projector augmented wave pseudopotentials were employed as implemented in VASP⁵⁸. A cutoff energy of 520 eV was set for all calculations, and the structures were allowed to relax until the total energy of the unit cell converged within 0.5 meV/atom between two ionic steps. To determine the stabilities of γ -brass phases where Li and Ag are disordered, various Li/Ag orderings were generated to evaluate the lowest energy configuration (Supplementary Table 1). *Pymatgen* was extensively used for this process⁵⁹.

Data availability

Source data are provided with this paper.

References

- Cheng, X.-B., Zhang, R., Zhao, C.-Z. & Zhang, Q. Toward safe lithium metal anode in rechargeable batteries: a review. *Chem. Rev.* **117**, 10403–10473 (2017).
- Lin, D., Liu, Y. & Cui, Y. Reviving the lithium metal anode for high-energy batteries. *Nat. Nanotechnol.* **12**, 194–206 (2017).
- Xu, W. et al. Lithium metal anodes for rechargeable batteries. *Energy Environ. Sci.* **7**, 513–537 (2014).
- Wen, J., Yu, Y. & Chen, C. A review on lithium-ion batteries safety issues: existing problems and possible solutions. *Mater. Express* **2**, 197–212 (2012).
- Liu, K., Liu, Y., Lin, D., Pei, A. & Cui, Y. Materials for lithium-ion battery safety. *Sci. Adv.* **4**, eaas9820 (2018).
- Janek, J. & Zeier, W. G. A solid future for battery development. *Nat. Energy* **1**, 16141 (2016).
- Manthiram, A., Yu, X. & Wang, S. Lithium battery chemistries enabled by solid-state electrolytes. *Nat. Rev. Mater.* **2**, 1–16 (2017).
- Huang, W.-Z. et al. Anode-free solid-state lithium batteries: a review. *Adv. Energy Mater.* **12**, 2201044 (2022).
- Heubner, C. et al. From lithium-metal toward anode-free solid-state batteries: current developments, issues, and challenges. *Adv. Funct. Mater.* **31**, 2106608 (2021).
- Yoon, G., Kim, S. & Kim, J.-S. Design strategies for anodes and interfaces toward practical solid-state Li-metal batteries. *Adv. Sci.* **10**, 2302263 (2023).
- Wang, M. J., Carmona, E., Gupta, A., Albertus, P. & Sakamoto, J. Enabling “lithium-free” manufacturing of pure lithium metal solid-state batteries through in situ plating. *Nat. Commun.* **11**, 5201 (2020).
- Lee, N., Oh, J. & Choi, J. W. Anode-less all-solid-state batteries: recent advances and future outlook. *Mater. Futures* **2**, 013502 (2023).
- Motoyama, M., Ejiri, M., Yamamoto, T. & Iriyama, Y. In situ scanning electron microscope observations of Li plating/stripping reactions with Pt current collectors on LiPON electrolyte. *J. Electrochem. Soc.* **165**, A1338–A1347 (2018).
- Kato, A., Hayashi, A. & Tatsumisago, M. Enhancing utilization of lithium metal electrodes in all-solid-state batteries by interface modification with gold thin films. *J. Power Sources* **309**, 27–32 (2016).
- Hiratani, M., Miyauchi, K. & Kudo, T. Effect of a lithium alloy layer inserted between a lithium anode and a solid electrolyte. *Solid State Ion.* **28–30**, 1406–1410 (1988).
- Kato, A. et al. High-temperature performance of all-solid-state lithium-metal batteries having Li/Li₃PS₄ interfaces modified with Au thin films. *J. Electrochem. Soc.* **165**, A1950–A1954 (2018).
- Wakasugi, J., Munakata, H. & Kanamura, K. Effect of gold layer on interface resistance between lithium metal anode and Li_{6.25}Al_{0.25}La₃Zr₂O₁₂ solid electrolyte. *J. Electrochem. Soc.* **164**, A1022–A1025 (2017).

18. Müller, A. et al. Influence of Au, Pt, and C Seed layers on lithium nucleation dynamics for anode-free solid-state batteries. *ACS Appl. Mater. Interfaces* **16**, 695–703 (2024).
19. Leite, M. S. et al. Insights into capacity loss mechanisms of all-solid-state Li-ion batteries with Al anodes. *J. Mater. Chem. A* **2**, 20552–20559 (2014).
20. Okita, K., Ikeda, K.-i, Sano, H., Iriyama, Y. & Sakaebe, H. Stabilizing lithium plating-stripping reaction between a lithium phosphorus oxynitride glass electrolyte and copper thin film by platinum insertion. *J. Power Sources* **196**, 2135–2142 (2011).
21. Fu, K. K. et al. Toward garnet electrolyte-based Li metal batteries: an ultrathin, highly effective, artificial solid-state electrolyte/metallic Li interface. *Sci. Adv.* **3**, e1601659 (2017).
22. Lee, Y.-G. et al. High-energy long-cycling all-solid-state lithium metal batteries enabled by silver-carbon composite anodes. *Nat. Energy* **5**, 299–308 (2020).
23. Kim, S. et al. High-power hybrid solid-state lithium-metal batteries enabled by preferred directional lithium growth mechanism. *ACS Energy Lett.* **8**, 9–20 (2023).
24. Kim, S. et al. High-energy and durable lithium metal batteries using garnet-type solid electrolytes with tailored lithium-metal compatibility. *Nat. Commun.* **13**, 1883 (2022).
25. Spencer-Jolly, D. et al. Structural changes in the silver-carbon composite anode interlayer of solid-state batteries. *Joule* **7**, 503–514 (2023).
26. Suzuki, N. et al. Highly cyclable all-solid-state battery with deposition-type lithium metal anode based on thin carbon black layer. *Adv. Energy Sustain. Res.* **2**, 2100066 (2021).
27. Kim, S. et al. The role of interlayer chemistry in Li-metal growth through a garnet-type solid electrolyte. *Adv. Energy Mater.* **10**, 1903993 (2020).
28. Wen, J. et al. A tailored interface design for anode-free solid-state batteries. *Adv. Mater.* **36**, 2307732 (2024).
29. Jin, S. et al. Solid-solution-based metal alloy phase for highly reversible lithium metal anode. *J. Am. Chem. Soc.* **142**, 8818–8826 (2020).
30. Ye, Y. et al. Solid-solution or intermetallic compounds: phase dependence of the Li-alloying reactions for Li-metal batteries. *J. Am. Chem. Soc.* **145**, 24775–24784 (2023).
31. Inaoka, T. et al. Tin interlayer at the Li/Li₃PS₄ interface for improved Li stripping/plating performance. *J. Phys. Chem. C* **127**, 10453–10458 (2023).
32. Lu, Y. et al. The void formation behaviors in working solid-state Li metal batteries. *Sci. Adv.* **8**, eadd0510 (2022).
33. Flavell, W. R. Spiers Memorial Lecture: prospects for photoelectron spectroscopy. *Faraday Discuss* **236**, 9–57 (2022).
34. Tsai, C.-L. et al. Li₇La₃Zr₂O₁₂ interface modification for Li dendrite prevention. *ACS Appl. Mater. Interfaces* **8**, 10617–10626 (2016).
35. Feng, W., Dong, X., Li, P., Wang, Y. & Xia, Y. Interfacial modification of Li/garnet electrolyte by a lithiophilic and breathing interlayer. *J. Power Sources* **419**, 91–98 (2019).
36. Wang, J. et al. Fundamental study on the wetting property of liquid lithium. *Energy Storage Mater.* **14**, 345–350 (2018).
37. Zhang, S. et al. Phase diagram determined lithium plating/stripping behaviors on lithiophilic substrates. *ACS Energy Lett.* **6**, 4118–4126 (2021).
38. Park, C.-M., Jung, H. & Sohn, H.-J. Electrochemical behaviors and reaction mechanism of nanosilver with lithium. *Electrochem. Solid State Lett.* **12**, A171–A175 (2009).
39. Li, B. et al. Dual protection of a Li–Ag alloy anode for all-solid-state lithium metal batteries with the argyrodite Li₆PS₅Cl solid electrolyte. *ACS Appl. Mater. Interfaces* **14**, 37738–37746 (2022).
40. Braga, M. H., Dębski, A., Terlicka, S., Gąsior, W. & Góral, A. Experimental and ab initio study of the Ag–Li system for energy storage and high-temperature solders. *J. Alloy. Compd.* **817**, 152811 (2020).
41. Fultz, B. *Phase Transitions in Materials* (Cambridge University Press, 2020).
42. Koo, B. et al. Dynamic surface phases controlling asymmetry of high-rate lithiation and delithiation in phase-separating electrodes. *Energy Environ. Sci.* **16**, 3302–3313 (2023).
43. Ravnsbæk, D. B. et al. Extended solid solutions and coherent transformations in nanoscale olivine cathodes. *Nano Lett.* **14**, 1484–1491 (2014).
44. Li, D. & Zhou, H. Two-phase transition of Li-intercalation compounds in Li-ion batteries. *Mater. Today* **17**, 451–463 (2014).
45. Wagemaker, M. et al. A kinetic two-phase and equilibrium solid solution in spinel Li_{4+x}Ti₅O₁₂. *Adv. Mater.* **18**, 3169–3173 (2006).
46. Binder, K. Theory of first-order phase transitions. *Rep. Prog. Phys.* **50**, 783–859 (1987).
47. Xia, Y., Xiong, Y., Lim, B. & Skrabalak, S. E. Shape-controlled synthesis of metal nanocrystals: simple chemistry meets complex physics? *Angew. Chem. Int. Ed.* **48**, 60–103 (2009).
48. Shi, F. et al. Strong texturing of lithium metal in batteries. *Proc. Natl Acad. Sci. USA* **114**, 12138–12143 (2017).
49. Bai, P., Li, J., Brushett, F. R. & Bazant, M. Z. Transition of lithium growth mechanisms in liquid electrolytes. *Energy Environ. Sci.* **9**, 3221–3229 (2016).
50. Lu, Y., Tu, Z. & Archer, L. A. Stable lithium electrodeposition in liquid and nanoporous solid electrolytes. *Nat. Mater.* **13**, 961–969 (2014).
51. Aurbach, D. et al. Attempts to improve the behavior of Li electrodes in rechargeable lithium batteries. *J. Electrochem. Soc.* **149**, A1267 (2002).
52. Steiger, J., Richter, G., Wenk, M., Kramer, D. & Mönig, R. Comparison of the growth of lithium filaments and dendrites under different conditions. *Electrochem. Commun.* **50**, 11–14 (2015).
53. Lee, J. et al. Room-temperature anode-less all-solid-state batteries via the conversion reaction of metal fluorides. *Adv. Mater.* **34**, e2203580 (2022).
54. Motoyama, M. et al. The active interface of Ta-doped Li₇La₃Zr₂O₁₂ for Li plating/stripping revealed by acid aqueous etching. *ACS Appl. Energy Mater.* **2**, 6720–6731 (2019).
55. Ma, C. et al. Excellent stability of a lithium-ion-conducting solid electrolyte upon reversible Li⁺/H⁺ exchange in aqueous solutions. *Angew. Chem. Int. Ed.* **54**, 129–133 (2015).
56. Notario-Estévez, A., Kozlov, S. M., Viñes, F. & Illas, F. Electronic-structure-based material descriptors: (in)dependence on self-interaction and Hartree–Fock exchange. *Chem. Commun.* **51**, 5602–5605 (2015).
57. Perdew, J. P. et al. Restoring the density-gradient expansion for exchange in solids and surfaces. *Phys. Rev. Lett.* **100**, 136406 (2008).
58. Blöchl, P. E. Projector augmented-wave method. *Phys. Rev. B Condens. Matter* **50**, 17953–17979 (1994).
59. Ong, S. P. et al. Python Materials Genomics (pymatgen): A robust, open-source python library for materials analysis. *Comput. Mater. Sci.* **68**, 314–319 (2013).

Acknowledgements

D.-S. Ko and S. Kim contributed equally to this work.

Author contributions

Dong-Su Ko: Conceptualization, Methodology, Investigation, Writing-Original Draft; Sewon Kim: Conceptualization, Investigation; Sangjun Lee: Investigation; Gabin Yoon: Investigation; Daeho Kim: Investigation; ChaeHo Shin: Investigation; Dongmin Kim: Investigation; Jaewoo Lee: Formal analysis; Soohwan Sul: Project administration; Dong-Jin Yun: Conceptualization, Methodology, Investigation; Changhoon Jung: Conceptualization, Methodology, Investigation. All authors contributed to the discussions.

Competing interests

The authors declare no competing interests.

Additional information

Supplementary information The online version contains supplementary material available at <https://doi.org/10.1038/s41467-025-55821-1>.

Correspondence and requests for materials should be addressed to Dong-Su Ko, Dong-Jin Yun or Changhoon Jung.

Peer review information *Nature Communications* thanks Bingyuan Ma, Munekazu Motoyama and the other, anonymous, reviewer(s) for their contribution to the peer review of this work. A peer review file is available.

Reprints and permissions information is available at <http://www.nature.com/reprints>

Publisher's note Springer Nature remains neutral with regard to jurisdictional claims in published maps and institutional affiliations.

Open Access This article is licensed under a Creative Commons Attribution-NonCommercial-NoDerivatives 4.0 International License, which permits any non-commercial use, sharing, distribution and reproduction in any medium or format, as long as you give appropriate credit to the original author(s) and the source, provide a link to the Creative Commons licence, and indicate if you modified the licensed material. You do not have permission under this licence to share adapted material derived from this article or parts of it. The images or other third party material in this article are included in the article's Creative Commons licence, unless indicated otherwise in a credit line to the material. If material is not included in the article's Creative Commons licence and your intended use is not permitted by statutory regulation or exceeds the permitted use, you will need to obtain permission directly from the copyright holder. To view a copy of this licence, visit <http://creativecommons.org/licenses/by-nc-nd/4.0/>.

© The Author(s) 2025